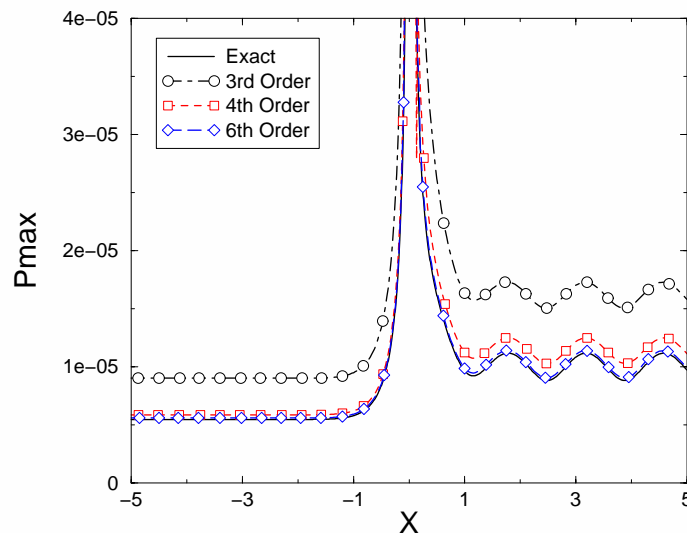




AIAA-2003-0880

High-Order Spectral Volume Method for Benchmark Aeroacoustic Problems

Z.J. Wang
Michigan State University
East Lansing, MI



41st Aerospace Sciences Meeting and Exhibit
6-9 January, 2003
Reno, Nevada

HIGH-ORDER SPECTRAL VOLUME METHOD FOR BENCHMARK AEROACOUSTIC PROBLEMS

Z.J. Wang[†]

Department of Mechanical Engineering
Michigan State University, East Lansing, MI 48824

ABSTRACT

A time accurate, high-order finite volume method named spectral volume (SV) method has been developed recently for conservation laws on unstructured grids. Each spectral volume is partitioned into control volumes (CVs), and cell-averaged state variable from these control volumes is used to reconstruct a high-order polynomial approximation in the spectral volume. Riemann solvers are used to compute the fluxes at spectral volume boundaries. Then cell-averaged state variables in the control volumes are updated independently. A very desirable feature of the SV method is that the reconstruction is identical for cells of the same type with similar partitions. In this study, the SV method is tested for several benchmark problems in computational aeroacoustics (CAA) to demonstrate its potential for CAA applications.

1. INTRODUCTION

A new finite volume method named the spectral volume (SV) method has been developed recently for hyperbolic conservation laws [1-2], and successfully demonstrated for both scalar and system conservation laws [3,4]. The goal set for developing the SV method has been to pursue a numerical method for conservation laws which has all of the following properties: a) conservative, b) high-order accuracy, i.e., the order of accuracy is greater than second order, c) geometrically flexible, i.e., applicable for unstructured grids, and d) computationally efficient. The SV method is developed to hopefully satisfy these four requirements, in a relative sense with respect to the current state-of-the-art numerical methods such as the high-order k-exact finite volume (FV) method [5], weighted essentially non-oscillatory (WENO) methods [6], the discontinuous Galerkin (DG) method [7,8], and the unstructured spectral method [9,10], amongst many others.

Ultimately, the SV method is a Godunov-type finite volume method [11], which has been under development for several decades, and has become the state-of-the-art for the numerical solution of hyperbolic conservation laws. For a more detailed review of the literature on the Godunov-type method, refer to [1], and the references therein. Similar to the Godunov method, the SV method has two key components. One is data reconstruction, and the other is the (approximate) Riemann solver. What distinguishes the SV method from the k-exact finite volume (FV) method is the data reconstruction. Instead of using a (large) stencil of

neighboring cells to perform a high-order polynomial reconstruction, the unstructured grid cell - called a spectral volume - is partitioned into a "structured" set of sub-cells called control volumes (CVs), and cell-averages on these sub-cells are then the degrees-of-freedom (DOFs). These DOFs are used to perform a high-order polynomial reconstruction inside the SV. All the spectral volumes are partitioned in a geometrically similar manner, and thus a single reconstruction is obtained. Next, the DOFs are updated to high-order accuracy using the usual Godunov method. Numerical tests with scalar conservation laws in both 1D and 2D have verified that the SV method is indeed highly accurate, conservative, and geometrically flexible [1-4].

In this paper, we test the SV method for several benchmark problems in computational aeroacoustics (CAA). As pointed out by Tam in [12], acoustic waves have their own characteristics which make their computation unique and challenging. Acoustic waves are inherently unsteady. Their amplitudes are several orders smaller than the magnitudes of the mean flow and their frequencies are generally very high and broad ranging. Computational methods with high order accuracy are required to capture the acoustic portion of the solution [13-17]. The requirement of geometric flexibility comes from the desire to compute noise over "real world" configurations, such as aircraft, or car geometries. Over the last decade, many high-order algorithms such as compact schemes [14], DRP (Dispersion-Relation Preserving) schemes [13] have been developed, and applied successfully in many CAA applications. These schemes were developed for

[†] Associate Professor (zjw@egr.msu.edu), AIAA Senior Member

Copyright © by Z.J. Wang, Published by the American Institute of Aeronautics and Astronautics Inc., with permission

Cartesian grid or smooth structured grids, and therefore the applications using these methods have limited to relatively simple geometries. For problems with complex geometries, it is a considerable challenge to generate any structured grid, let alone a smooth structured grid, which can preserve the high-order accuracy of the numerical algorithms. We, therefore, advocate an unstructured grid approach for complex configurations.

The paper is organized as follows. In the next section, we first present the SV method for the two dimensional Euler equations. Then multi-dimensional limiters necessary for non-linear Euler equations with discontinuities are described. After that, we discuss several issues for the quasi-one-dimensional Euler equations. In Section 5, three CAA benchmark cases, two 1D and one 2D, are presented. Finally, conclusions and recommendations for further investigations are summarized in Section 6.

2. SPECTRAL (FINITE) VOLUME METHOD FOR 2D EULER EQUATIONS

The unsteady 2D Euler equation in conservative form can be written as

$$\frac{\partial Q}{\partial t} + \frac{\partial E}{\partial x} + \frac{\partial F}{\partial y} = 0, \quad (1)$$

where Q is the vector of conserved variables, E and F are the inviscid flux vectors given below:

$$Q = \begin{Bmatrix} \rho \\ \rho u \\ \rho v \\ E \end{Bmatrix}, \quad E = \begin{Bmatrix} \rho u \\ \rho u^2 + p \\ \rho uv \\ u(E + p) \end{Bmatrix}, \quad F = \begin{Bmatrix} \rho v \\ \rho uv \\ \rho v^2 + p \\ v(E + p) \end{Bmatrix}. \quad (2)$$

Here ρ is the density, u and v are the velocity components in x and y directions, p is the pressure, and E is the total energy. The pressure is related to the total energy by

$$E = \frac{p}{\gamma - 1} + \frac{1}{2} \rho (u^2 + v^2), \quad (3)$$

with ratio of specific heats $\gamma = 1.4$ for air. The Jacobian matrix for the flux vector in an arbitrary direction $\mathbf{n} = (n_x, n_y)$ can be written as

$$B = n_x \frac{\partial E}{\partial Q} + n_y \frac{\partial F}{\partial Q}.$$

B has 4 real eigenvalues $\lambda_{1,2} = v_n$, $\lambda_3 = v_n + c$, $\lambda_4 = v_n - c$, and a complete set of (right column) eigenvectors $\{r_1, r_2, r_3, r_4\}$, where $v_n = un_x + vn_y$ and c is the speed of sound. Let R be the matrix composed of these right eigenvectors, then the Jacobian matrix B can be diagonalized as

$$R^{-1}BR = \Lambda, \quad (4)$$

where Λ is the diagonal matrix containing the eigenvalues, i.e.,

$$\Lambda = \text{diag}(v_n, v_n, v_n + c, v_n - c). \quad (5)$$

Assume that we solve (1) in computational domain Ω subject to proper initial and boundary conditions. Domain Ω is discretized into N non-overlapping triangular elements called spectral volumes (SVs)

$$\Omega = \bigcup_{i=1}^N S_i. \quad (6)$$

Given a desired order of accuracy k for (1), each spectral volume S_i is then partitioned into $m = k(k+1)/2$ control volumes (CVs), and the j -th CV of S_i is denoted by $C_{i,j}$. Several convergent partitions of various degrees are shown in Figure 1. Let q denote any of the conservative variables in Q . The cell-averaged conservative variable q at time t for control volume $C_{i,j}$ is defined as

$$\bar{q}_{i,j}(t) = \frac{\int_{C_{i,j}} q(x, y, t) dV}{V_{i,j}} \quad (7)$$

where $V_{i,j}$ is the volume of $C_{i,j}$. Given the cell-averaged conservative variables for all the CVs in S_i , a polynomial $p_i(x, y) \in P^{k-1}$ (the space of polynomials of degree at most $k-1$) can be reconstructed such that it is a k -th order accurate approximation to the function $q(x, y)$ inside S_i :

$$p_i(x, y) = q(x, y) + O(h^k), \quad (x, y) \in S_i, \quad (8)$$

This reconstruction can be solved analytically by satisfying the following conditions:

$$\frac{\int_{C_{i,j}} p_i(x,y) dV}{V_{i,j}} = \bar{q}_{i,j}, \quad j = 1, \dots, m. \quad (9)$$

This polynomial $p_i(x,y)$ is the k -th order approximation we are looking for as long as the function $q(x,y)$ is smooth in the region covered by S_i . The reconstruction can be more conveniently expressed as

$$p_i(x,y) = \sum_{j=1}^m L_j(x,y) \bar{q}_{i,j}, \quad (10)$$

where $L_j(x,y) \in P^{k-1}$ are the "shape" functions which satisfy

$$\frac{\int_{C_{i,j}} L_m(x,y) dV}{V_{i,j}} = \delta_{jm}. \quad (11)$$

The high-order reconstruction is then used to generate high-order updates for the cell-averaged state variable on the CVs. Integrating (1) in $C_{i,j}$, we obtain the following integral equation for the CV-averaged mean

$$\frac{d\bar{Q}_{i,j}}{dt} + \frac{1}{V_{i,j}} \sum_{r=1}^K \int_{A_r} (f \bullet \mathbf{n}) dA = 0, \quad (12)$$

where $\bar{Q}_{i,j}$ is the vector of the CV-averaged conservative variables in $C_{i,j}$, $f = (E, F)$, K is the number of faces in $C_{i,j}$, and A_r represents the r -th face of $C_{i,j}$. The surface integral on each face can be performed with a k -th order accurate Gauss quadrature formula, i.e.

$$\int_{A_r} (f \bullet \mathbf{n}) dA = \sum_{q=1}^J w_{rq} f(Q(x_{rq}, y_{rq})) \bullet \mathbf{n}_r A_r + O(A_r h^k), \quad (13)$$

where $J = \text{integer}[(k+1)/2]$ is the number of quadrature points on the r -th face and, w_{rq} are the Gauss quadrature weights, (x_{rq}, y_{rq}) are the Gauss quadrature points, h is the maximum edge length of all the CVs. If $f = \text{constant}$, the following identity exists:

$$\sum_{r=1}^K \int_{A_r} (f \bullet \mathbf{n}) dA = 0. \quad (14)$$

Therefore, we will gain an extra order of accuracy if we sum up the surface integrals for the faces of $C_{i,j}$, i.e.,

$$\sum_{r=1}^K \int_{A_r} (f \bullet \mathbf{n}) dA = \sum_{r=1}^K \sum_{q=1}^J w_{rq} f(Q(x_{rq}, y_{rq})) \bullet \mathbf{n}_r A_r + O(A_r h^{k+1}). \quad (15)$$

Since $O(V_i) = O(A_r h)$, we therefore have

$$\frac{1}{V_{i,j}} \sum_{r=1}^K \int_{A_r} (f \bullet \mathbf{n}) dA = \frac{1}{V_{i,j}} \sum_{r=1}^K \sum_{q=1}^J w_{rq} f(Q(x_{rq}, y_{rq})) \bullet \mathbf{n}_r A_r + O(h^k). \quad (16)$$

With the polynomial distribution on each SV , the state variable is most likely discontinuous across the SV boundaries. Therefore, the flux integration involves two discontinuous state variables just to the left and right of a face of the SV boundary. This flux integration is carried out using an exact Riemann solver or one of the Lipschitz continuous approximate Riemann solvers or flux splitting procedures, i.e.,

$$f(Q(x_{rq}, y_{rq})) \bullet \mathbf{n}_r \approx \hat{f}(Q_L(x_{rq}, y_{rq}), Q_R(x_{rq}, y_{rq}), \mathbf{n}_r), \quad (17)$$

where Q_L and Q_R are the vector of conserved variables just to the left and right of a face. Substituting (17) into (13), we obtain

$$\int_{A_r} (f \bullet \mathbf{n}) dA = \sum_{q=1}^J w_{rq} \hat{f}(Q_L(x_{rq}, y_{rq}), Q_R(x_{rq}, y_{rq}), \mathbf{n}_r) A_r + O(A_r h^k). \quad (18)$$

It is the Riemann solver which introduces the "upwinding", and dissipation into the SV method such that the SV method is not only high-order accurate, but also stable. In this paper, we employ the Roe Riemann solver [18]

$$\hat{f}(Q_L, Q_R, \mathbf{n}) = \frac{1}{2} [f(Q_L) + f(Q_R) - |\bar{B}|(Q_R - Q_L)], \quad (19)$$

where $|\bar{B}|$ is the dissipation matrix computed from

$$|\bar{B}|_{i,j+1/2} = R |\bar{\Lambda}| R^{-1}. \quad (20)$$

Here $|\bar{\Lambda}|$ is the diagonal matrix composed of the absolute values of the eigenvalues of the Jacobian matrix evaluated at the so-called Roe-averages, i.e.,

$$\bar{B} = B(Q^A), \quad (21)$$

and R is also evaluated at the Roe averages [18].

Finally we obtain the following semi-discrete SV scheme

$$\begin{aligned} \frac{d\bar{Q}_{i,j}}{dt} + \\ \frac{1}{V_{i,j}} \sum_{r=1}^K \sum_{q=1}^J w_{rq} \hat{f}(Q_L(x_{rq}, y_{rq}), Q_R(x_{rq}, y_{rq}), \mathbf{n}_r) A_r = 0. \end{aligned} \quad (22)$$

For time integration, we use the third-order TVD Runge-Kutta scheme from [19]. We first rewrite (22) in a concise ODE form

$$\frac{d\bar{Q}}{dt} = R_h(\bar{Q}), \quad (23)$$

Then the third-order TVD Runge-Kutta scheme can be expressed as:

$$\begin{aligned} \bar{Q}^{(1)} &= \bar{Q}^n + \Delta t R_h(\bar{Q}^n); \\ \bar{Q}^{(2)} &= \frac{3}{4} \bar{Q}^n + \frac{1}{4} [\bar{Q}^{(1)} + \Delta t R_h(\bar{Q}^{(1)})]; \\ \bar{Q}^{n+1} &= \frac{1}{3} \bar{Q}^n + \frac{2}{3} [\bar{Q}^{(2)} + \Delta t R_h(\bar{Q}^{(2)})]. \end{aligned} \quad (24)$$

3. MULTI-DIMENSIONAL TVD AND TVB LIMITERS

For the non-linear Euler equations, it is necessary to perform data limiting to maintain stability if the solution contains discontinuities. TVD limiters enforce strict monotonicity by sacrificing solution accuracy at local extrema, while TVB limiters relax the monotonicity requirement to achieve uniform accuracy away from discontinuities. In this paper, both limiters are presented in a uniform TVB limiter form, with TVD being a special case. There are two different ways of applying limiters in the system setting. One way is to apply a limiter to each characteristic variable. The other is to apply a limiter to each component of the vector of the conservative variables. The former has the nice property of naturally degenerating to the scalar case if the hyperbolic system is linear, but the latter is much more efficient. In this paper, we choose the component-wise approach because of its efficiency. To this end, we

first establish the following numerical monotonicity criterion for each control volume

$$\bar{q}_{i,j}^{\min} \leq q_{i,j}(x_{rq}, y_{yq}) \leq \bar{q}_{i,j}^{\max}, \quad (25)$$

where $\bar{q}_{i,j}^{\min}$ and $\bar{q}_{i,j}^{\max}$ are the minimum and maximum cell-averaged solutions among all its neighboring CVs sharing a face with $C_{i,j}$, i.e.,

$$\begin{aligned} \bar{q}_{i,j}^{\max} &= \max(\bar{q}_{i,j}, \max_{1 \leq r \leq K} \bar{q}_{i,j,r}) \\ \bar{q}_{i,j}^{\min} &= \min(\bar{q}_{i,j}, \min_{1 \leq r \leq K} \bar{q}_{i,j,r}), \end{aligned} \quad (26)$$

and $q_{i,j}(x_{rq}, y_{yq})$ is the reconstructed solution at any of the quadrature points. It was proven by Liu [20] in the scalar case that if (25) is satisfied by the reconstruction, the numerical solution satisfies a maximum principle, i.e., the solution is monotonic. If (25) is strictly enforced, the resultant numerical scheme for the scalar case is TVD. However, it is well known that TVD schemes are locally first-order at extrema, and may degrade the global accuracy of the solution. In order to maintain the order of accuracy away from discontinuities, the TVB idea [7] is followed here, i.e., small oscillations are allowed in the solution. If we express the reconstruction for the quadrature points in the following form

$$\Delta q_{rq} = p_i(x_{rq}, y_{yq}) - \bar{q}_{i,j},$$

then no data limiting is necessary if

$$|\Delta q_{rq}| \leq 4M_q h_{rq}^2, \quad (27)$$

where $h_{rq} = |\mathbf{r}_{i,j} - \mathbf{r}_{rq}|$ is the distance from the CV centroid to the quadrature point. In other words, no data limiting is necessary if (27) is satisfied, even if (25) is not. Usually the constant M_q is chosen to be the maximum second derivative of the solution. However M_q is a user chosen parameter if there is a discontinuity in the solution. Note that a different M_q should be used for a different conservative variable. In this paper, M_q is scaled according to the minimum and maximum of the component, i.e.,

$$M_q = M(q_{\max} - q_{\min}). \quad (28)$$

where M is a constant independent of the component, and q_{\max} and q_{\min} are the maximum and minimum of the solution q over the computational domain. If (25) is violated for any quadrature point, then it is assumed

that the CV is close to a discontinuity, and the solution in the CV is locally linear, i.e.,

$$q_{i,j}(x, y) = \bar{q}_{i,j} + \nabla q_{i,j} \bullet (\mathbf{r} - \mathbf{r}_{i,j}), \quad \forall \mathbf{r} \in C_{i,j}. \quad (29)$$

The magnitude of the solution gradient is maximized subject to the monotonicity condition given in (25). The original high-order reconstruction in the CV is used to compute an initial guess of the gradient, i.e.,

$$\nabla q_{i,j} = \left(\frac{\partial p_m}{\partial x}, \frac{\partial p_m}{\partial y} \right) \Big|_{\mathbf{r}_{i,j}}.$$

This gradient may not satisfy (25). Therefore it is limited by multiplying a scalar $\varphi \in [0, 1]$ so that the following solution satisfies (25)

$$q_{i,j}(x, y) = \bar{q}_{i,j} + \varphi \nabla q_{i,j} \bullet (\mathbf{r} - \mathbf{r}_{i,j}). \quad (30)$$

The scalar can be computed from

$$\varphi = \begin{cases} \min \left(1, \frac{\Delta q_{rq}}{\bar{q}_{i,j}^{\max} - \bar{q}_{i,j}} \right) & \text{if } \Delta q_{rq} > 0 \\ \min \left(1, \frac{\Delta q_{rq}}{\bar{q}_{i,j}^{\min} - \bar{q}_{i,j}} \right) & \text{if } \Delta q_{rq} < 0. \\ 1 & \text{otherwise} \end{cases} \quad (31)$$

In the case of $M = 0$, the limiter becomes TVD. The availability of cell-averaged data on the CVs inside a SV makes this CV-based data limiting possible, whereas in the *DG* method, one can only do an element based data limiting. Due to the increased local resolution, the *SV* method was shown to have better resolutions for discontinuities than the *DG* method [3]. This advantage should also carry over to the multi-dimensional systems case.

Note that at the interior CV boundaries inside a SV, the reconstructed conservative variables are continuous if no limiter is imposed. Then the flux is just the analytical flux, which is cheaper to compute than the Riemann flux.

4. QUASI-ONE DIMENSIONAL EULER EQUATIONS

The degeneration from the 2D Euler equations to the quasi-1D equations is obvious. The 1D equations have

a source term in the momentum equation due to the variation in the cross-section area, as evident in the following form

$$\frac{\partial Q}{\partial t} + \frac{\partial E}{\partial x} = G, \quad (32a)$$

where:

$$Q = \begin{Bmatrix} \rho \\ \rho u \\ E \end{Bmatrix}, E = \begin{Bmatrix} \rho u \\ \rho u^2 + p \\ u(E + p) \end{Bmatrix}, G = \begin{Bmatrix} -\rho u \frac{1}{A} \frac{\partial A}{\partial x} \\ -\rho u^2 \frac{1}{A} \frac{\partial A}{\partial x} \\ \frac{u(E + p)}{A} \frac{\partial A}{\partial x} \end{Bmatrix}, \quad (32b)$$

where A is the cross section area. The computational domain is first subdivided into N SVs. Each SV is further partitioned into k CVs, according to the Gauss-Lobatto mapping. The j -th CV in the i -th SV is then $C_{ij} = (x_{i,j-1/2}, x_{i,j+1/2})$. The integration of (32) in C_{ij} gives

$$\frac{d\bar{Q}_{i,j}}{dt} h_{i,j} + (E_{i,j+1/2} - E_{i,j-1/2}) = \int_{x_{i,j-1/2}}^{x_{i,j+1/2}} G dx, \quad (33)$$

where $h_{i,j} = x_{i,j+1/2} - x_{i,j-1/2}$. The integration of the source term is again performed with a Gauss quadrature formula of suitable order of accuracy with an analytical area derivative.

5. NUMERICAL TESTS

5.1 Sound Waves through a Transonic Nozzle

This case is selected from the Third Computational Aeroacoustics (CAA) Workshop on Benchmark Problems [21]. A one-dimensional nozzle with the following area distribution is considered

$$A(x) = \begin{cases} 0.536572 - 0.198086e^{-\ln 2(x/0.6)^2}, & x > 0 \\ 1.0 - 0.661514e^{-\ln 2(x/0.6)^2}, & x < 0 \end{cases}.$$

The computational domain is $[-10, 10]$. The mean flow is completely subsonic with an exit Mach number of 0.4. Small amplitude acoustics waves, with angular frequency $\omega = 0.6\pi$, is generated way downstream and propagate upstream through the narrow passage of the nozzle throat. The acoustic wave in the uniform region downstream of the nozzle can be represented by

$$\begin{bmatrix} \rho' \\ u' \\ p' \end{bmatrix} = \varepsilon \begin{bmatrix} 1 \\ -1 \\ 1 \end{bmatrix} \cos \left[\varpi \left(\frac{x}{1-M} + t \right) \right],$$

where $\varepsilon = 1.e-5$. The non-linear Euler equations were employed in the simulation. Therefore we need to first compute the mean flow solution.

In the initial test, only uniform grids were employed in order to remove the effects of the grid from the consideration. Three SV schemes with 3rd, 4th and 6th order of accuracy were investigated with the same degrees of freedom (DOFs). Therefore, 200, 150, and 100 SVs were used for the 3rd, 4th and 6th order schemes respectively, resulting in a total of 600 DOFs. Characteristic boundary conditions were used in both the inlet and exits based on the propagating directions of the waves. The mean flow solutions from all three schemes are plotted in Figure 2. Note that the solutions agree very well with each other, indicating that the mean flow solution is scheme and grid-independent. The mean flow solution was then used as the initial condition for the unsteady simulation. The unsteady upstream-propagating acoustic waves are imposed directly on the right side of the downstream boundary face, with the left side state variables reconstructed from the interior domain. The Riemann solver automatically takes care of the wave propagation. The unsteady solution reached periodic after $t = 40$. The maximum acoustic pressure is then determined over several periods. The maximum acoustic pressures computed with the SV schemes are compared with the analytical solution in Figure 3. As expected, the 6th order scheme performs much better than the 3rd and 4th order schemes with the same DOFs. The computed instantaneous acoustic pressure distributions are compared with the analytical solution in Figure 4. Again, the 6th order SV scheme performs the best.

Since the acoustic waves have much higher frequencies near the throat than those in the constant area downstream region, a better computational mesh can be produced by clustering the grid points near the throat. Such a mesh with 30 SVs was generated, and the maximum SV is about 20 times larger than the minimum SV. The 6th order SV scheme was then employed on this non-uniform mesh to carry out the same simulation with 180 DOFs. The computed maximum acoustic pressure is compared with the analytical solution in Figure 5, which also displays the computational mesh. For comparison purposes, the computed maximum acoustic pressures on both the uniform and non-uniform grids are compared with the analytical solution in Figure 6. With only 180 DOFs, the computed acoustic pressure on the non-uniform grid

agrees better than that on the uniform grid with 600 DOFs. Finally the computed instantaneous pressure is plotted with the analytical solution in Figure 7. They are right on top of each other.

5.2 Shock-Sound Interaction

This case is again selected from the Third Computational Aeroacoustics (CAA) Workshop on Benchmark Problems. The nozzle geometry is the same as in the previous case. The mean flow is supersonic at the inlet, and the exit pressure is so designed that a shock wave is generated downstream of the throat. At the inflow boundary, the conditions are:

$$\begin{bmatrix} \rho \\ u \\ p \end{bmatrix} = \begin{bmatrix} 1 \\ M \\ 1/\gamma \end{bmatrix} + \varepsilon \begin{bmatrix} 1 \\ 1 \\ 1 \end{bmatrix} \sin \left[\varpi \left(\frac{x}{1+M} - t \right) \right],$$

where $\varepsilon = 1.e-5$, $\omega = 0.6\pi$, $M_{inlet} = 0.2006533$. The exit pressure is set to be 0.6071752 to create a shock. A uniform grid with 100 SVs and the 2nd order SV scheme were used in the simulation. Although higher-order SV schemes were tried, it appeared that the limiters had a detrimental effect on the acoustic waves. Designing acoustic-wave preserving limiters will be a future research topic. The computed mean pressure is compared with the analytical solution in Figure 8. The agreement is good, though the numerical solution is slightly oscillatory. It would be interesting to see whether this small oscillation affects the acoustic waves. The computed instantaneous acoustic pressure is displayed with the analytical solution in Figure 9. It seems the small oscillation does not seriously affect the acoustic waves, and the acoustic waves are free to propagate across the shock wave. The pressure history at the exit is plotted in Figure 10 with the analytical solution. Generally speaking, the agreement is very good.

5.3 Vortex Evolution Problem

This is an idealized problem for the Euler equations in 2D used by Shu [15]. The mean flow is $\{\rho, u, v, p\} = \{1, 1, 1, 1\}$. An isotropic vortex is then added to the mean flow, i.e., with perturbations in u , v , and temperature $T = p/\rho$, and no perturbation in entropy $S = p/\rho^\gamma$:

$$\begin{aligned} (\delta u, \delta v) &= \frac{\varepsilon}{2\pi} e^{0.5(1-r^2)} (-\bar{y}, \bar{x}), \\ \delta T &= -\frac{(\gamma-1)\varepsilon^2}{8\gamma\pi^2} e^{1-r^2}, \\ \delta S &= 0, \end{aligned}$$

where $(\bar{x}, \bar{y}) = (x - 5, y - 5)$, $r^2 = \bar{x}^2 + \bar{y}^2$, and the vortex strength $\varepsilon = 5$. The computational domain is $[0, 10] \times [0, 10]$. In the numerical simulation, we wish to test the SV schemes for handling the long time evolution of the vortex. For this purpose, periodic boundary conditions were employed at all the boundaries. The simulation was performed on a regular grid with $20 \times 20 \times 2$ SVs, which is displayed in Figure 11. Figure 12 shows the density profiles along $x = 5$ at $t = 0, 10, 50$ and 100 for the second, third and fourth order SV schemes. Note that the second-order SV scheme displays significant dispersion and dissipation error, especially for the long term simulations. In contrast, both the third-order and fourth-order schemes give excellent results. The computed pressure contours at $t = 100$ are compared with the exact solution in Figure 13, which again reinforces the conclusion that high order schemes produced significantly better results.

CONCLUSIONS

The SV method has been tested on several benchmark CAA problems in this paper. It is clearly demonstrated that high-order schemes are required to deliver the expected solution accuracy in CAA problems, and they do perform much better than lower order ones. It is also found that limiters have a detrimental effect on the acoustic waves. Acoustic wave preserving limiters are necessary for the high-order schemes to handle shock-sound wave interactions efficiently, and this will be a future research topic.

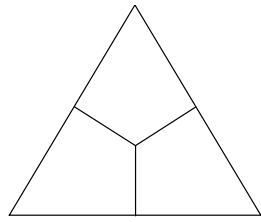
ACKNOWLEDGEMENT

The author gratefully acknowledges the Intramural Research Grant Project awarded by Michigan State University, and the start-up funding provided by the Department of Mechanical Engineering, College of Engineering of Michigan State University.

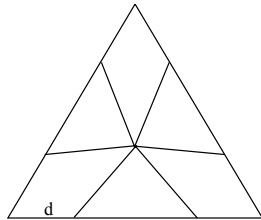
REFERENCES

1. Z.J. Wang, and Y. Liu, "Spectral (Finite) Volume Method for Conservation Laws on Unstructured Grids II: Extension to Two-Dimensional Scalar Equation", *J. Computational Physics*, Vol. 179, pp. 665-697, 2002.
2. Z.J. Wang, "Spectral (Finite) Volume Method for Conservation Laws on Unstructured Grids: Basic Formulation", *J. Computational Physics*, Vol. 178, pp. 210-251, 2002.
3. Z.J. Wang and Y. Liu, "Spectral (Finite) Volume Method for Conservation Laws on Unstructured Grids III: Extension to One-Dimensional Systems", under review.
4. Z.J. Wang, L. Zhang and Y. Liu, "Spectral (Finite) Volume Method for Conservation Laws on Unstructured Grids IV: Extension to Two-Dimensional Euler Equations", under review.
5. T.J. Barth and P.O. Frederickson, High-order solution of the Euler equations on unstructured grids using quadratic reconstruction," AIAA Paper No. 90-0013, 1990.
6. C. Hu and C.-W. Shu, "Weighted essentially non-oscillatory schemes on triangular meshes," *J. Comput. Phys.* **150**, 97-127 (1999).
7. B. Cockburn, S. Hou and C.-W. Shu, TVB Runge-Kutta local projection discontinuous Galerkin finite element method for conservation laws IV: the multidimensional case, *Mathematics of Computation* **54**, 545-581 (1990).
8. F. Bassi and S. Rebay, High-order accurate discontinuous finite element solution of the 2D Euler equations, *J. Comput. Phys.* **138**, 251-285 (1997).
9. J.S. Hesthaven and C.H. Teng, "Stable Spectral Methods On Tetrahedral Elements," *SIAM J. Sci. Comput.* **21**, 2352-2380 (2000).
10. G.E. Karniadakis and S.J. Sherwin, "Spectral/hp Element Methods in CFD," Oxford University Press, 1999.
11. S.K. Godunov, A finite-difference method for the numerical computation of discontinuous solutions of the equations of fluid dynamics, *Mat. Sb.* **47**, 271 (1959).
12. C.K.W. Tam, "Computational Aeroacoustics: Issues and Methods," AIAA Journal, Vol. 33, No. 10, Oct. 1995, pp. 1788-1796.
13. C.K.W. Tam and J.C. Webb, "Dispersion-Relation-Preserving Finite difference Schemes for Computational Acoustics," *J. Comput. Phys.*, Vol. 107, No. 2, Aug. 1993, pp. 262-281.
14. S.K. Lele, "Compact Finite Difference Schemes with Spectral-Like Resolution," *J. Comput. Phys.*, Vol. 103, 1992, pp. 16-42.
15. C.-W. Shu, "High Order Finite-Difference And Finite Volume WENO Methods And Discontinuous Galerkin Methods For CFD," ICASE Report 2001-11, 2001.
16. A.T. Patera, "A Spectral Element Method For Fluid Dynamics: Laminar Flow In A Channel Expansion," *J. Comput. Phys.* **54** 468-488 (1984).
17. D.A. Kopriva and J.H. Koliass, "A Conservative Staggered-Grid Chebyshev Multidomain Method For Compressible Flows," *J. Comput. Phys.* **125**, 244 (1996).
18. P.L. Roe, Approximate Riemann solvers, parameter vectors, and difference schemes, *J. Comput. Phys.* **43** 357-372 (1981).

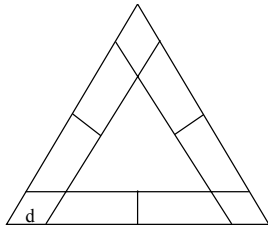
19. C.-W. Shu, Total-Variation-Diminishing time discretizations, *SIAM Journal on Scientific and Statistical Computing* **9**, 1073-1084 (1988).
20. X.D. Liu, A maximum principle satisfying modification of triangle based adaptive stencil for the solution of scalar hyperbolic conservation laws, *SIAM J. Numer. Anal.* **30**, 701-716 (1993).
21. C.K.W. Tam, L.N. Sankar, and D.L. Huff, "Third Computational Aeroacoustics (CAA) Workshop on Benchmark Problems", Nov. 8-10, 1999.



(a) Linear SV



(b) Quadratic SV



(c) Cubic SV

Figure 1. SVs of various degrees

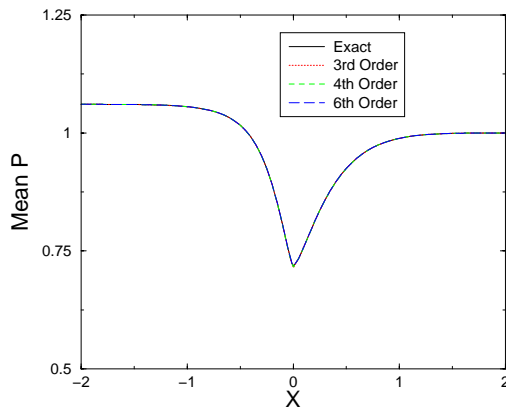


Figure 2. Computed and analytical mean pressures for the subsonic flow through a converging-diverging nozzle

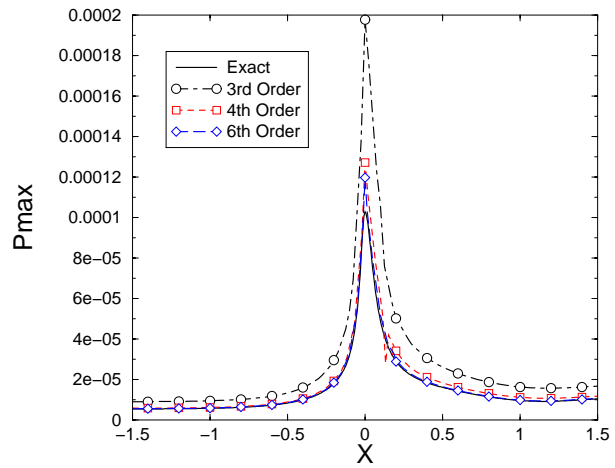
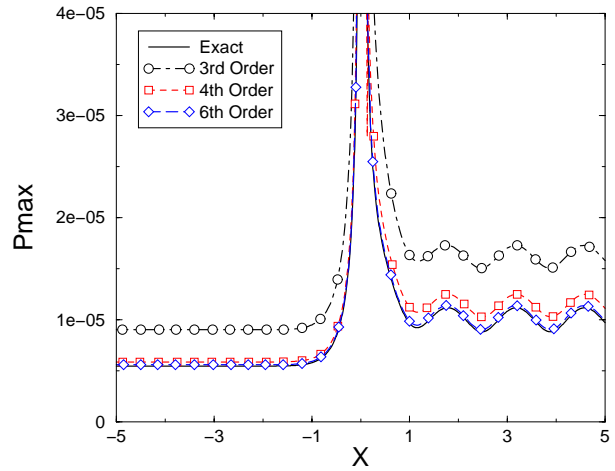


Figure 3. Comparison of computed and exact maximum acoustic pressures

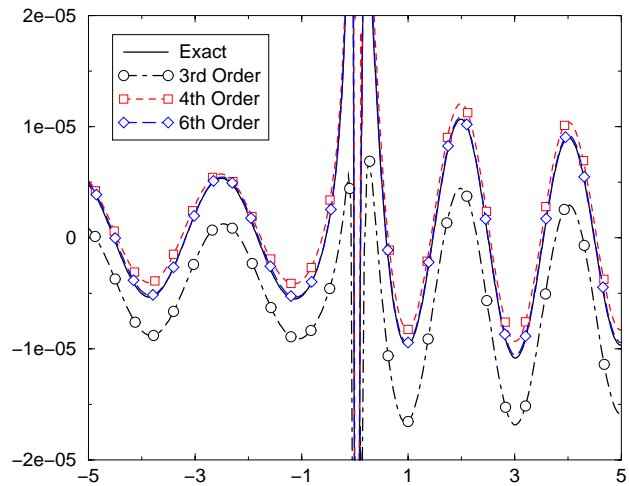


Figure 4. Comparison of computed and exact instantaneous acoustic pressures

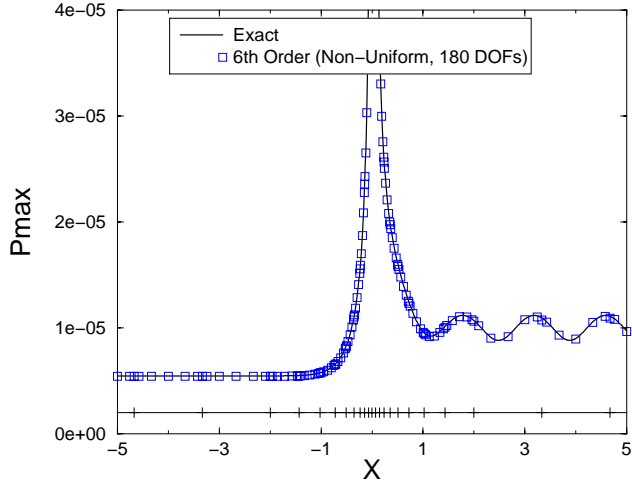


Figure 5. Computed maximum acoustic pressure on the non-uniform grid, with comparison to the exact solution

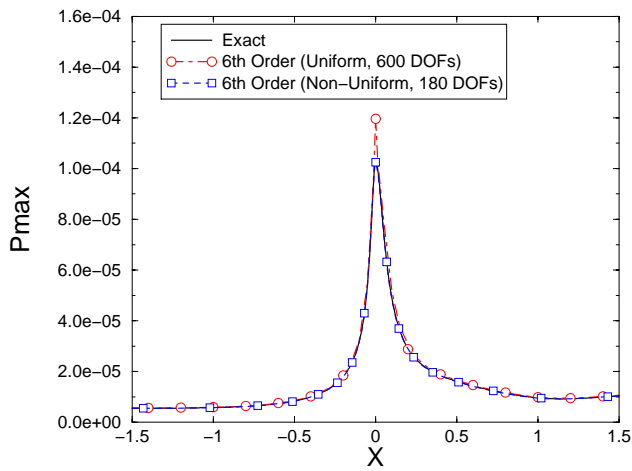


Figure 6. Computed maximum acoustic pressures on both the uniform and non-uniform grids

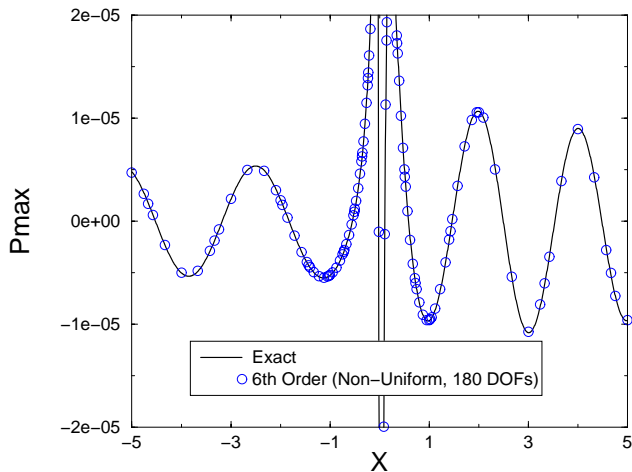


Figure 7. Comparison of computed and exact instantaneous acoustic pressures

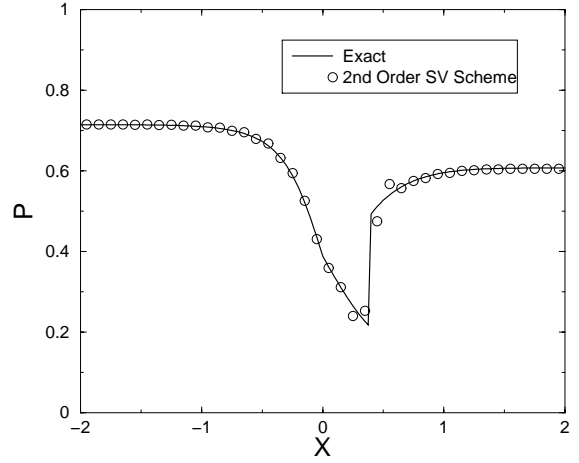


Figure 8. Computed and analytical mean pressures for the supersonic flow through a laval nozzle

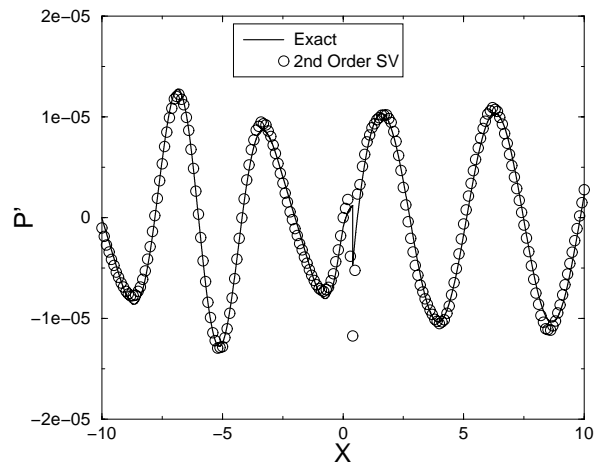


Figure 9. Comparison of computed and exact instantaneous acoustic pressures

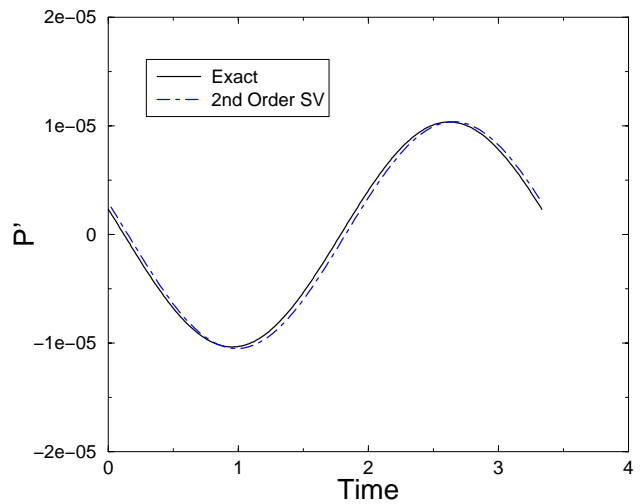


Figure 10. Comparison of pressure histories at the nozzle exit

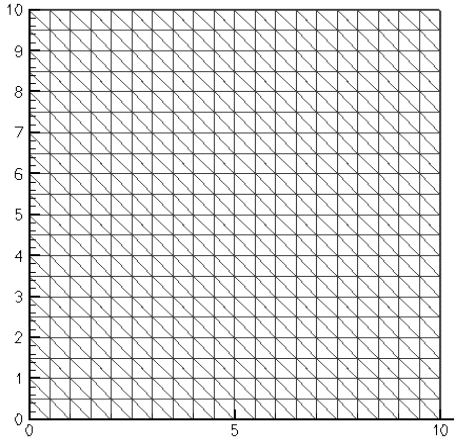
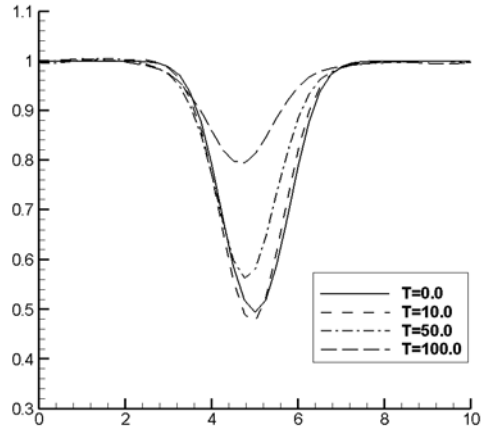
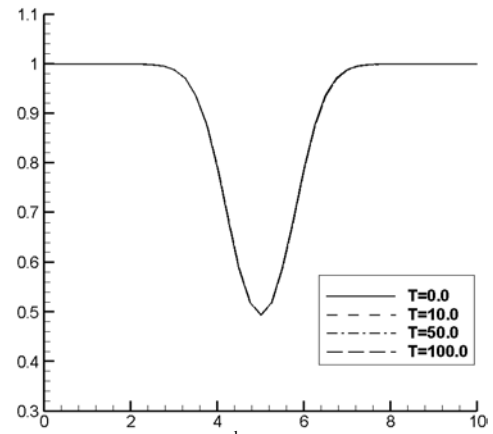


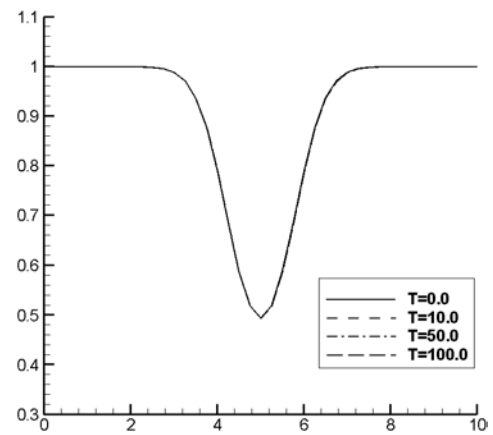
Figure 11. Regular "20x20x2" Computational Grids



(a) 2nd Order

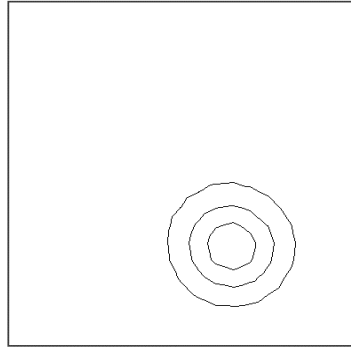


(b) 3rd Order

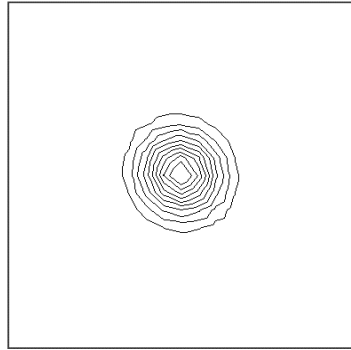


(c) 4th Order

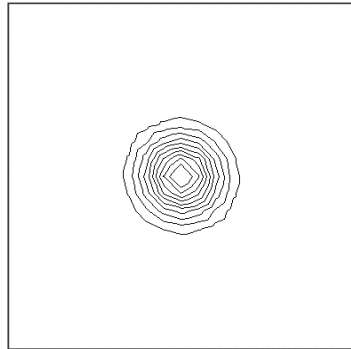
Figure 12. Density profiles along $x=5$ at $t=0, 10, 50$ and 100 for the second, third and fourth order SV schemes



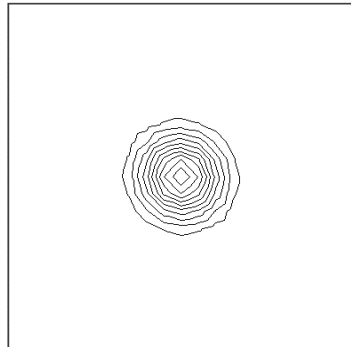
(a) 2nd Order



(b) 3rd Order



(c) 4th Order



(d) Exact

Figure 13. Pressure Contours at $t = 100$